ACS Photonics

Article

pubs.acs.org/journal/apchd5

Tailoring Second-Harmonic Generation in Single L-Shaped Plasmonic Nanoantennas from the Capacitive to Conductive Coupling Regime

Leo-Jay Black,[†,§] Peter R. Wiecha,[‡,§] Yudong Wang,[†] C. H. de Groot,[⊥] Vincent Paillard,[‡] Christian Girard,[‡] Otto L. Muskens,[*,†] and Arnaud Arbouet[*,‡]

[†]Physics and Astronomy, and [⊥]Nano Group, Faculty of Physical Sciences and Engineering, University of Southampton, Highfield, Southampton SO17 1BJ, United Kingdom

[‡]CEMES, UPR 8011, CNRS-Université de Toulouse, 29 Rue Jeanne Marvig, BP 94347, F-31055 Toulouse, France

Supporting Information

ABSTRACT: We investigate the efficiency of second-harmonic generation (SHG) over the transition from capacitive to conductive coupling in orthogonal L-shaped dimer gold antennas. By tuning both the gap and antenna length, the bonding and antibonding resonances are individually addressed. Results on the intensity and polarization of SHG are compared quantitatively with microscopic numerical simulations taking into account the nanoscale nonlinear surface dipole distribution, elucidating the interplay between symmetry at macroscopic and microscopic levels and optical resonance effects. Microscopic modeling reveals strong cancellations of nonlinear dipoles by capacitive coupling in plasmonic nanogaps, resulting in only small changes in SHG efficiency despite large local field enhancement in the gap. Experimentally, irreproducible polarization properties are obtained in a range of parameters associated with strong optical near fields in the gap of the antennas, which is interpreted as a consequence of nanoscopic asymmetries inherited from the fabrication process. Our results demonstrate that nanoscopic defects can either strongly impact the nonlinear optical emission or have a barely detectable influence depending on the excited optical resonance and associated optical near-field distribution. These results provide useful design rules to optimize the design of nonlinear plasmonic nanostructures.

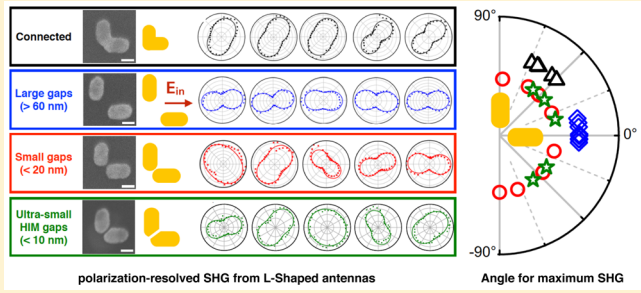

KEYWORDS: *second-harmonic generation, SHG, plasmonics, nanoantennas, polarization conversion, metasurface*

Metallic nanoantennas supporting surface plasmon (SP) resonances efficiently convert free radiation fields into localized oscillating electric fields.[1−3] This ability to confine and enhance the electric field has placed these nanostructures at the heart of many applications such as plasmon-enhanced spectroscopy,[4] controlling light directivity,[5] and photodetection.[6] Concentration of optical fields is even more important when considering nonlinear optical interactions, as the latter are more sensitive to the electric field strength. The influence of surface plasmons on second-harmonic generation (SHG),[7−13] third-harmonic generation (THG),[14,15] four-wave mixing (FWM),[16] and strong-field photoemission[17] has been clearly demonstrated, and a lot of effort has been put into the design of metallic nanostructures with optimized nonlinear properties.[18] In order to enhance nonlinear conversion efficiency, designs such as doubly resonant[19] or multiresonant plasmonic nanostructures[20,21] and metallic nanostructures supporting Fano resonances[22,23] have been investigated. It has been shown that plasmonic nanostructures can enhance the nonlinearities of their constituent metal,[21,24−26] but they can also boost or switch nonlinear light emission from their surrounding.[27−29] Enhanced nonlinear optical response has now been proposed for a variety of applications, among which detection of optically trapped nanoparticles,[30,31] high-resolution near-field imaging,[32] modulation and switching,[33] or coherent control of light scattering.[34]

Integration of single nanoantennas into ultrathin, planar optical metasurfaces has raised great interest for the potential of altering the phase and polarization of electromagnetic waves, with applications such as flat lenses, meta-holograms, and polarization elements.[35−38] Whereas initial studies were aimed at achieving new linear optical properties, research efforts now address the nonlinear response of these nanostructured plasmonic surfaces.[39−42] It has been shown that the efficiency of harmonic generation can be strongly influenced by the geometric arrangement of elements in a metasurface.[40,43] Next to these collective effects, a precise understanding of nonlinear light emission in the optical near field of a single nanoantenna is necessary to optimize the nonlinear conversion efficiency of individual nanoantennas and metasurfaces. In particular, whereas the nonlinear optical response of a nanostructure generally benefits from the enhancement of its linear response,

Received: June 30, 2015
Published: October 19, 2015

DOI: 10.1021/acsphotonics.5b00358
ACS Photonics 2015, 2, 1592−1601

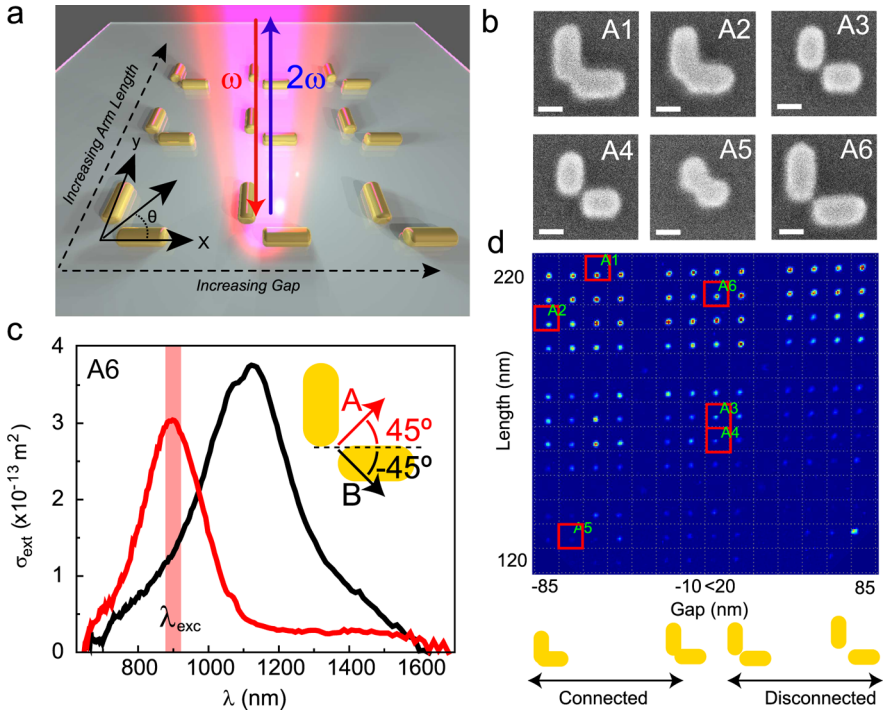

Figure 1. (a) Orthogonal gold dimer antennas deposited on a glass substrate (n_s = 1.5). (b) SEM images of several antennas identified on d (scale bar = 100 nm). (c) Scattering spectrum measured on a disconnected antenna showing the antibonding and bonding modes (respectively A and B). (d) Raw SHG spatial intensity map acquired on an entire array with an incident *E*-field at 900 nm polarized along the antibonding axis. The squares are used for antenna identification and data processing.

the electric fields induced at the fundamental and harmonic frequencies can have different symmetries.[19,44] Cancellation of nonlinear dipoles only nanometers apart can therefore result in a complete silencing of the SHG in these structures.[44] From a general point of view, the influence of optical resonances and symmetries at both macroscopic and microscopic levels has been pointed out in the literature.[44−49] However, these combined effects depend sensitively on design parameters such as resonance length and feed gap, and disentangling their respective influence is necessary to draw efficient design rules for nonlinear nanostructures. Furthermore, fundamental limitations in fabrication techniques such as e-beam lithography strongly affect the results of SHG experiments and their agreement with theoretical models.[47]

Here, we investigate second-harmonic generation from both conductively and capacitively coupled L-shaped gold antenna dimers, focusing on the intensity and polarization of the emitted SHG for different resonance conditions. The geometry of the orthogonal dimer was chosen for its direct relationship to linear dimer antennas,[44] however with an important difference that both the bonding and antibonding hybridized modes of the orthogonal dimers are radiative. In comparison, cancellation of the linear dipoles produces a dark, nonradiating antibonding mode in the parallel dimer antenna. The possibility of optically addressing the symmetry properties of the nonlinear susceptibility has motivated several studies of SHG from L-shaped antennas.[7,48,50,51] The combined influence of geometrical effects and local field distribution has been pointed out in the case of SHG from arrays of T-shaped nanostructures.[42] Beside these two important factors, the additional role of surface plasmon resonances on SHG from metallic nano-objects needs to be systematically investigated.

In this context, our current study brings together several important elements by (i) covering a wide range of single antennas designed to address both bonding and antibonding resonances, (ii) analyzing these antennas through quantitative single-particle extinction spectroscopy and nonlinear optical microscopy to precisely attribute the response, and (iii) interpreting the results through extensive electrodynamical simulations. Exploring a complete parameter space of optical excitation and antenna morphology (gap, length) over the transition from conductive coupling to capacitive coupling allows us to disentangle the influence of local field enhancement, particle macroscopic symmetry, and local microscopic symmetry on the SHG.

Our experimental results are compared with numerical simulations of the SHG emitted by an L-shaped antenna. The nonlinear scattering model is based on the assumption that only electric field components normal to the nanoparticle surface contribute to the nonlinear polarization,[8,41,47,52] as is discussed in more detail in Supporting Information Section S3. While there is still an open debate on which components to assume for best describing the SHG process in gold nanoantennas, this approach has been used with very good results in the case of far-field SHG microscopy.[8,21,41,47,52] More complex experiments such as SHG near-field microscopy, in which the interaction of the emitted SHG with the environment is expected to have a strong influence, could demand more complex theoretical approaches.[53] In particular, a time-domain implementation of the hydrodynamic model has been recently developed to provide a nonperturbative description of the nonlinear coherent interaction between light and plasmonic nanostructures.[54] This sophisticated model provides a self-consistent numerical solution, free from any approximation,

DOI: 10.1021/acsphotonics.5b00358
ACS Photonics 2015, 2, 1592−1601

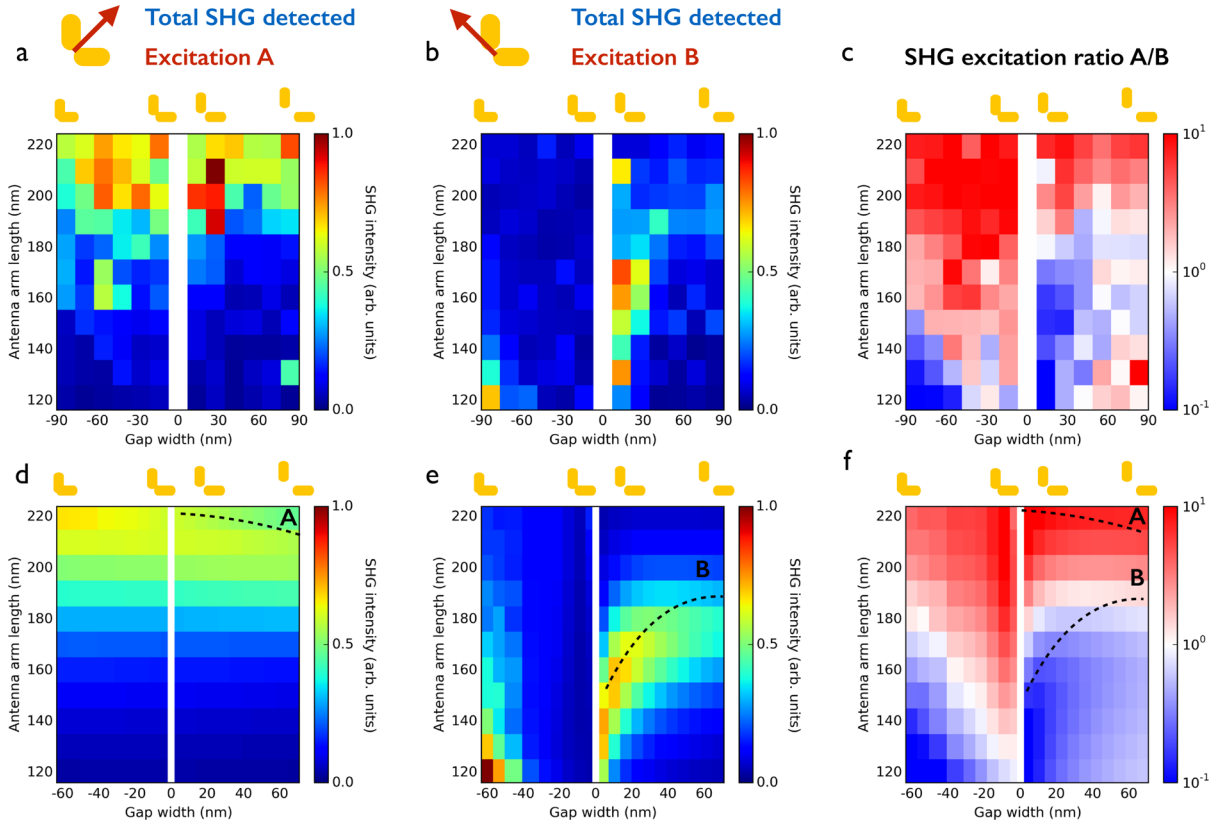

Figure 2. (a) Total detected SHG for an incident *E*-field at 900 nm and linearly polarized at 45° (A-axis). (b) Same for an excitation at −45° (B-axis). (c) Ratio of A/B excitation efficiencies obtained from a and b. (d, e) Calculated excitation efficiency corresponding to geometries of a and b, with (f) calculated ratio of A/B excitation efficiencies, for internal fields 5 nm below the nanoparticle surface. The dashed lines correspond to the condition of resonant excitation of the antibonding (d) or bonding (e) mode of the antennas deduced from antenna cross-section calculations detailed in Supporting Information Figure S4.

which is more accurate, in particular for the description of the near-field distribution of the nonlinear sources.

While many of the observed dependencies are successfully explained by the microscopic description of the nonlinear surface dipole distribution over a large range of antenna dimensions, deviations from the theoretical behavior show up for strong capacitive coupling in large fluctuations of the polarization properties of the SHG emission. These effects are attributed in our work to a large energy concentration in the gap region combined with nanoscale local asymmetries, which cause imperfect silencing of SHG.

RESULTS AND DISCUSSION

Figure 1a shows the principle of the experiment. L-shaped antennas, composed of two gold rods of equal length L (L between 120 and 220 nm) and thickness t = 50 nm, were fabricated by electron beam lithography on a glass substrate (see Experimental Section). By systematically varying the gap width, two different situations have been investigated, in which the antenna arms are either conductively or capacitively coupled. The antennas were fabricated in a square array with a mutual spacing of 4 μm, large enough to prevent interparticle electromagnetic interactions. Figure 1b shows SEM images of several representative antennas, which will be investigated in detail in the following. The linear optical properties of all the antennas investigated in this work have first been characterized by spatial modulation spectroscopy using a setup optimized for detection in the infrared spectral range[55,56] (see Supporting Information Section S1). Figure 1c shows extinction spectra of a disconnected antenna consisting of two nanorods of 200 nm length with a gap of around 12 ± 5 nm. For linearly polarized incident light with polarizations of −45° and 45° (respectively labeled as B-axis and A-axis in the following), we observe different optical resonances, the low- and high-energy modes corresponding to the bonding (B) and antibonding (A) modes, respectively, as defined by the charge distributions of the modes.[36,37] For the selected antenna A6, the antibonding mode A overlaps with the femtosecond laser excitation wavelength at 900 nm.

Following the linear spectroscopic characterization, we measured the SHG emission over the entire array. The second harmonic generated by single nanoantennas was studied using a Ti:Sa femtosecond laser oscillator at a wavelength of 900 nm (see Supporting Information Section S2). The investigated antennas were placed on a nanopositioning stage and raster scanned in the laser beam focus (NA = 0.8). The incident power at the back of the microscope objective was kept constant at 1 mW, corresponding to an average intensity of 10^5 W/cm^2, while the polarization of the incident light could be controlled using a half-wave plate. Light generated at the second-harmonic frequency was collected in epi-collection configuration with a dichroic mirror and SHG bandpass filter and was detected using a photon multiplier in photocurrent mode. In part of the experiments, the polarization of the SHG was analyzed using a polarizer placed in front of the detector.

Figure 1d shows an SHG spatial intensity map for an incident polarization along the A-axis and unpolarized detection. For

DOI: 10.1021/acsphotonics.5b00358
ACS Photonics 2015, 2, 1592−1601

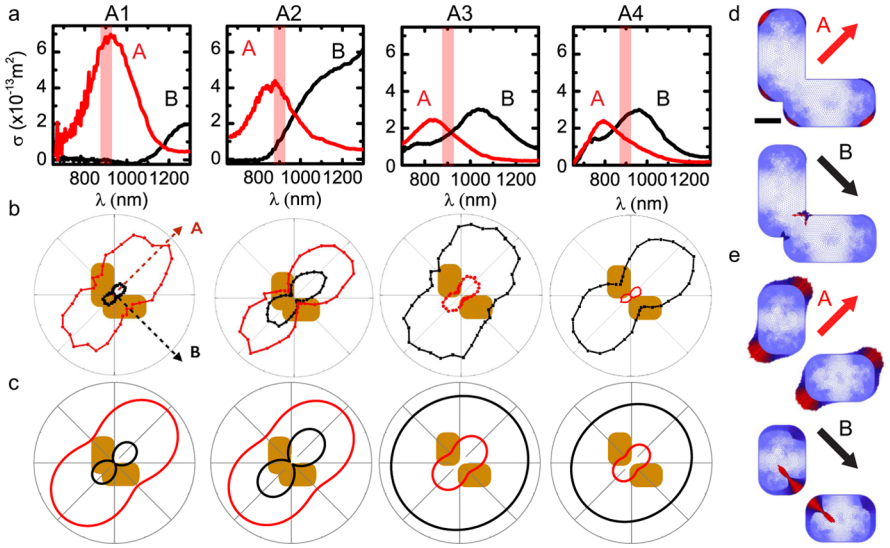

Figure 3. Extinction cross sections (a) and polarization-resolved SHG intensity (b) for selected antennas A1−A4. SHG was measured at 900 nm fundamental wavelength. (c) Calculated polarization-resolved SHG intensity for antenna geometries corresponding to b, for excitation polarized along A (45°, antibonding configuration, red) and along B (−45°, bonding configuration, black). (d, e) Corresponding dipole distributions (red arrows) for A1 (d) and A3 (e) for A and B polarizations. Color scale indicates vector length increasing from blue to red.

each antenna, the total SHG intensity in Figure 1d was integrated over the spot area and plotted as a single value, resulting in the corresponding two-dimensional parameter map shown in Figure 2a. The SHG intensities collected when the antennas were excited with incident polarization along the B-axis are shown in Figure 2b. Both maps were normalized to the highest intensity found in the configuration of Figure 2a. For polarization along A, the highest intensities of SHG are obtained for antennas with arm lengths in the 180−200 nm range, corresponding to the resonant excitation of the antibonding mode at 900 nm. When the polarization of the incident wave is rotated to the B-axis, a different set of antennas produced the highest SHG, as shown in Figure 2b. This situation corresponds to a resonant excitation of the bonding mode, as can be seen from single-particle extinction spectra such as shown in Figure 3a and in Supporting Information Figure S2. These results clearly show that the SHG is resonantly enhanced by the plasmon resonance at the excitation wavelength. As shown in Supporting Information Figure S4, the wavelength of the antibonding mode is not much affected by the gap width, and therefore the excitation efficiencies of the antennas in Figure 2d do not change much with gap spacing. The situation is very different in Figure 2e. In this case, the wavelength of the bonding mode is strongly dependent on the gap width and the SHG efficiency clearly varies a lot with gap. We note that the bottom left group of connected antennas around L = 130 nm, G = −80 nm (antenna A5 in Figure 1b) closely resembles a single nanorod positioned at an angle of −45° (B-axis) with a longitudinal resonance wavelength overlapping with the pump wavelength, which explains the additional resonant enhancement in this area. While Figure 2a and b emphasize the response of antennas with the highest intensities, additional information on excitation efficiency over a wider range of parameters is obtained by taking the ratio of the SHG intensities obtained in the A and B configurations, shown in Figure 2c. Even for antennas with low SHG yield, the ratio between the two polarizations is well-defined, and a transition in excitation polarization efficiency occurs between the A and B resonances (more information about signal-to-noise ratio in our experiment is provided in the Supporting Information Section S2). Similar results are found for different arrays with nominally the same design parameters (see Supporting Information Figure S7), within the intrinsic limitations of the e-beam fabrication tolerances (±10 nm).

Model results are shown in Figures 2d−f for the normal component of the nonlinear polarization $\chi^{(2)}_{nnn}$, while a comprehensive presentation of the other surface components $\chi^{(2)}_{npp}$ and $\chi^{(2)}_{ppn}$ is given in Supporting Information Section S3.2. The normal component quantitatively describes most of the experimental observations. It predicts the enhancement of SHG following the A and B resonances and the flipping of the A/B intensity ratio (visible as a transition from red to blue colors in Figure 2c and f). A very similar response is calculated for $\chi^{(2)}_{ppn}$ (Figure S11), while $\chi^{(2)}_{npp}$ does not show agreement at all with experimental data. These calculations serve to compare qualitative behaviors and assume equal material susceptibilities. However, their absolute contribution critically depends on the magnitudes of the normal and tangential nonlinear material susceptibilities, which as yet are unknown. Therefore, it is not possible to include all three tensor components into a single SHG response.

Notably, reducing the gap from 60 nm down to <20 nm results in only a factor of ∼2 increase of the SHG intensity at resonance for the bonding mode, while the corresponding near-field enhancement in the gap region exceeds more than an order of magnitude (see Supporting Information Figure S3). As will be discussed in more detail below, this is a consequence of the cancellation of most of the nonlinear field components in the gap region, resulting in a strongly silenced SHG.

Next to the excitation characteristics of Figure 2, a full polarization analysis was done for selected antennas A1−A4, corresponding to the condition that an eigenmode is resonantly excited with the appropriate wavelength and polarization. Figure 3a shows the corresponding extinction spectra, and the polarization-resolved SHG intensity is shown in Figure 3b. Antennas resonant with the antibonding mode (A1 and A2) show a stronger overal SHG intensity for the A excitation condition, while the antennas resonant with the bonding mode

DOI: 10.1021/acsphotonics.5b00358
ACS Photonics 2015, 2, 1592−1601

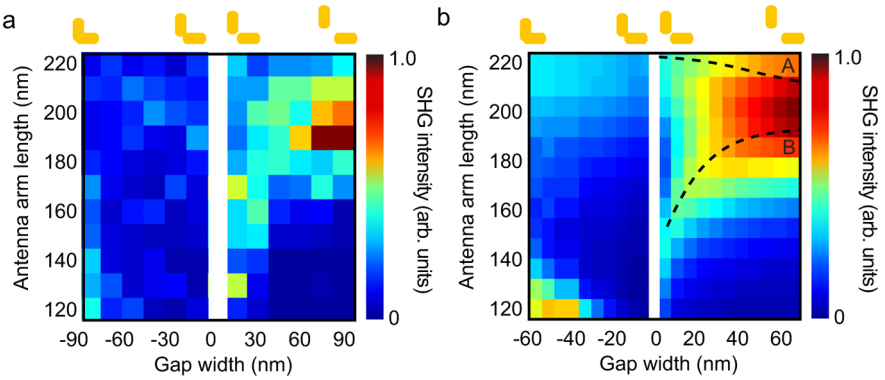

Figure 4. (a) Total detected SHG for an incident *E*-field at 900 nm and linearly polarized at 0° (horizontal). (b) Computed total SHG in the same configuration as a.

(A3 and A4) show a stronger SHG for the B excitation condition. Despite these variations in excitation efficiency consistent with Figure 2, excitation along either A or B results in SHG emission polarized predominantly along the symmetry axis of the L-shaped antennas, i.e., the A-axis. This behavior is confirmed by global studies of emission intensity along A and B directions, shown in Supporting Information Figures S9 and S10.

The calculated relative intensities and polarizations of SHG, shown in Figure 3c, are in general good agreement with the experimental results, with some deviation mainly for the bonding modes of A3 and A4, where the experiment shows a more polarized emission along A than the calculation. The fact that the SHG is polarized along A even for an excitation along B can be understood at a microscopic level by considering the fact that the distribution of the nonlinear sources that are ultimately responsible for the second-harmonic emission can have a very different symmetry from that of the fundamental *E*-field.[19,42] In particular, whereas the electric field for a resonant excitation of the bonding (B) mode is antisymmetric with respect to the symmetry axis of the antennas, the polarization induced at 2ω in each antenna arm is symmetric and flipped with respect to ω, resulting in a total nonlinear polarization orthogonal to the incident polarization. This effect is illustrated in Figure 3d,e which shows the distribution of induced dipoles at the second-harmonic frequency corresponding to antennas A1 (d) and A3 (e). Large nonlinear dipoles are created at resonance for small gaps for the B mode. For ideal geometries, these nonlinear sources in the gap cancel[44] and the remaining SHG is polarized along the symmetry axis of the antennas.

Selection rules can also be inferred from the global symmetry of the nonlinear susceptibility tensor $\chi^{(2)}$.[49] For the L-shape geometry, it reduces to C_{1v} when the substrate−air asymmetry is taken into account.[7,45] The only in-plane nonzero tensor elements for these symmetries are $\chi^{(2)}_{AAA}$, $\chi^{(2)}_{ABB}$, $\chi^{(2)}_{BAB}$, and $\chi^{(2)}_{BBA}$, where the first index indicates the SHG polarization and the latter two indices represent the polarizations of the two incident fields. For incident fields along either A or B only, the individual tensor elements $\chi^{(2)}_{AAA}$ and $\chi^{(2)}_{ABB}$ are addressed and SHG is polarized along A in both cases. The A/B ratio in Figure 2c thus directly gives the ratio of the susceptibilities $\chi^{(2)}_{AAA}/\chi^{(2)}_{ABB}$. In the case of a resonant excitation of the antibonding mode, the measured ratio is consistent with previous results obtained in the same configuration.[50] The scaling of the $\chi^{(2)}$ elements is furthermore in qualitative agreement with the nonlinear oscillator model, which predicts that the nonlinear susceptibility is proportional to the product of the linear susceptibilities of the two incident fields, $\chi^{(2)}_{ijk} \propto |\chi^{(1)}_j \chi^{(1)}_k|$.[7,9] According to this model, the nonlinear susceptibility is expected to follow the bonding and antibonding resonances for incident light along B and A, respectively.

Exploring a wide parameter space of antenna gaps and lengths allows us to monitor the gradual transition from L-shaped to more symmetric structures and the associated change of symmetry group. This is clearly the case for antennas with short arm lengths, such as antenna A5 shown in Supplementary Figure S10. Here, the SHG emission is predominantly polarized along B. This behavior is consistent with the fact that the morphology of these antennas is very close to a nanorod oriented at −45° (B-axis).[9] However, even for "normal" L-shaped antennas such as A3 and A4, it can be seen that both the experimental and calculated SHG emission at resonance is not fully polarized along the predicted symmetry direction (A-axis), but a significant fraction is emitted along the B-axis polarization, which shows that full electrodynamic calculations are essential to understand the detailed SHG polarization distribution.

The case of SHG excitation along A and B is of interest, as it allows selective driving of the pure eigenstates of the L-shaped antenna, providing a measurement of the individual $\chi^{(2)}$ tensor elements associated with these modes. A different regime is provided by excitation along one of the antenna arms, where directions A and B are equally excited. In the linear case, excitation along X has been shown to result in gap-dependent effects such as polarization conversion.[37] In an intuitive picture, driving along one antenna arm should lead to SHG polarized along this antenna for large gaps, while near-field coupling will set up a more complex superposition of eigenstates for small capacitive gaps and for connected antennas.

Figure 4a shows the absolute intensity for excitation along X. Markedly, the highest SHG is not obtained for the smallest capacitive gaps, but rather for uncoupled antennas. The reason for this difference is the fact that for small gaps only the pure B mode contributes to the SHG, which is excited with only half of the intensity in Figure 4. For large gaps, both the A and B modes are degenerate and both modes therefore contribute to the SHG for horizontal excitation, resulting in a larger overall intensity than for small-gap antennas. The case of polarization along X therefore shows that the SHG intensity is not primarily governed by the near-field enhancement associated with narrow gaps, which can be attributed to strong silencing effects, as will be discussed further below.

DOI: 10.1021/acsphotonics.5b00358
ACS Photonics 2015, 2, 1592−1601

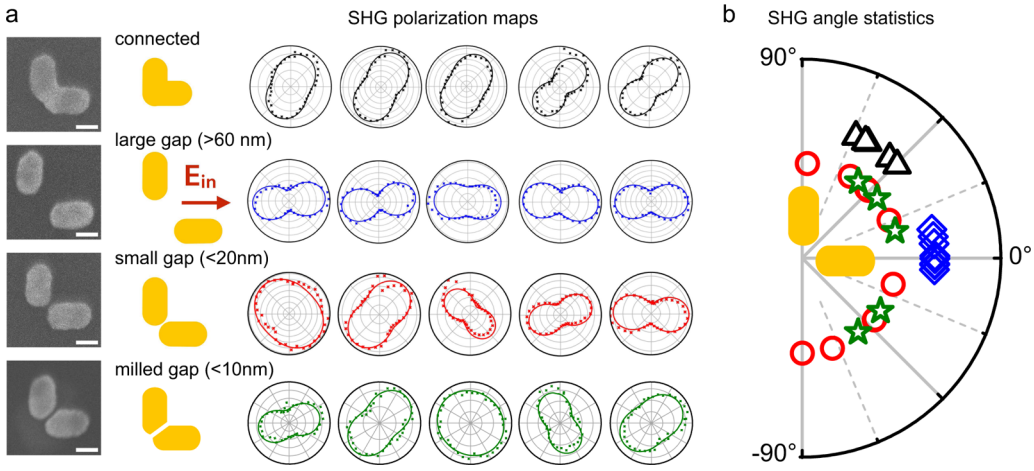

Figure 5. (a) Examples of polarization-resolved SHG intensities measured on different connected (upper row), disconnected with large gaps (second row), disconnected with small (<20 nm) gaps (third row), and ultrasmall helium ion milled gaps (bottom row), for an incident *E*-field along X. (b) Statistics of the angles for maximum SHG for the three different morphologies (colors corresponding to respective rows).

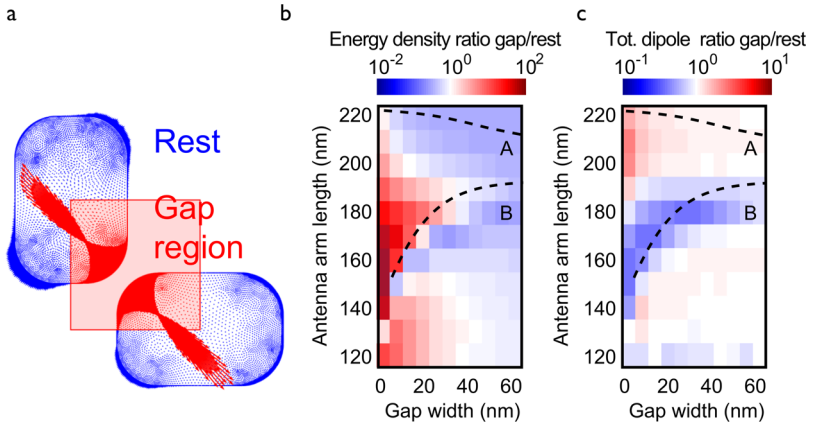

Figure 6. (a) Nonlinear polarization distribution induced by an optical excitation at 900 nm, for an incident *E*-field along X. Definition of the gap vs nongap region for the computation of the SHG contributions. (b) Ratio of energy density in the gap region to the exterior of the gap region. (c) Ratio of the total dipole moment in the gap region to the exterior of the gap region.

The emission polarization for excitation along the horizontal antenna is further investigated by taking a number of full polarization maps for selected antennas. Figure 5a shows polarization-resolved SHG intensities for four conditions corresponding to disconnected antennas with large gaps (>20 nm), small gaps (<20 nm), ultrasmall gaps (<10 nm), and connected rods (gap <0 nm). The ultrasmall gaps were fabricated by helium ion beam milling of connected antennas (see Experimental Section). Both the cases of conductively coupled antennas and capacitively coupled antennas with large gaps yield very reproducible results. The former consistently generate an SHG polarized along A, whereas the latter yield an SHG polarized parallel to the fundamental wave. The situation of capacitively coupled antennas with small and ultrasmall gaps is more complex, and, as shown in Figure 5b, the measurements performed on 15 different antennas with nominally the same design morphologies have produced very different results.

This extreme sensitivity of the SHG polarization to the gap width is illustrated in Figure 6, showing the calculated weight of the nonlinear sources arising from dipoles located in the gap. For this purpose, we individually analyzed the total energy and net dipole moment of the gap region, defined as the quadrant of the antennas closest to the gap, and the rest of the antenna (see Figure 6a). The results displayed in Figure 6b show that the fraction of energy contained in the gap in the regime of small gaps is several orders of magnitude larger than in the rest of the antenna. However, as can be seen in Figure 6c, the net dipole is strongly suppressed because of cancellation of dipoles of opposite sign. As more energy is drawn into the gap, the cancellation of nonlinear dipoles is enhanced, and therefore the SHG is reduced for smaller gaps at resonance. Thus, despite the strong field enhancement, capacitive nanogaps are generally not advantageous for the SHG efficiency.

Very importantly, the exact cancellation of the nonlinear dipoles strongly depends on the details of the shape of the antenna gap. As the gap width is decreased, the nonlinear polarization dramatically increases in the gap region due to the strong local electric fields (Figure 6a), and the local symmetry of the gap region directly dictates the ability of the nonlinear dipole distribution to cancel. Compared to the symmetric nanostructures considered in the theoretical calculations, the structures obtained using lithography and/or helium ion milling are generally not ideal and contain deviations from perfect local symmetry. Similar effects were observed in numerical studies where the polarization of SHG for a single linear nanoantenna was found to depend strongly on nanoscale morphology.[47] Here, we show that the influence of local asymmetry due to local defects in the gap morphology is not so important if the

DOI: 10.1021/acsphotonics.5b00358
ACS Photonics 2015, 2, 1592−1601

optical near fields in the gap are small, as is the case for large gaps, or for small gaps in the antibonding configuration. However, the effect of small irregularities is strongly increased in the case of enhanced optical near fields in the gap (see Figure 2b).

The precise mapping of SHG for a wide range of antenna lengths and gaps and for different polarizations has enabled direct characterization of the various modes on the SHG response. The resonant enhancement of SHG follows the resonance conditions at the fundamental wavelength, in agreement with the anharmonic oscillator model. Comparison with microscopic modeling shows how local field distributions and cancellation of nonlinear sources in the near field produce a macroscopic response in agreement with group theory over a range of parameters. However, the macroscopic symmetry rules lose validity when the nanoantenna parameters are gradually scaled away from the L-shape geometry toward a different point symmetry, while the microscopic model correctly predicts the properties in this regime.

An important point, which was already pointed out in several studies, but which is still cause for misunderstandings in the field, is that the overall emitted SHG intensity does not increase with local field enhancement for a locally symmetric nanogap. On the contrary, increased concentration of energy in the gap region means that effectively the SHG is more strongly suppressed for narrow gaps by exact cancellation of local dipoles. In reality, such silencing is never perfect in nanofabricated structures, resulting in an unpredictable and strongly varying SHG response in both intensity and polarization even for high-quality e-beam and HIM structures as presented in this study. Our results show that nonlinear emission from nanostructures of fixed macroscopic symmetry can present very different robustness with respect to fabrication imprecision depending on the excited optical resonance and associated optical near-field topography. This extreme sensitivity of the SHG polarization to local defects in the gap region is a limitation for the complete control of SHG for strongly coupled orthogonal antennas and will impact, for example, the use of plasmonic gap antennas for nonlinear metasurfaces. Such sensitivities of SHG to local defects were pointed out in other studies.[46,47,51] Our current work specifically addresses the combined interplay of strong interactions and optical resonance and shows that the influence of local defects depends strongly on the excited optical resonance and associated optical near-field distribution.

Provided that better control on a sub-20 nm gap is achieved, orthogonal plasmonic antennas could provide original platforms in which the coupling strength between the two antenna arms and its modification upon a change in the dielectric properties of the gap region are detected through a modification of both the intensity and polarization of the emitted SHG. Such enhanced control may be provided by alternative fabrication techniques such as helium ion beam milling to improve SHG control in plasmonic nanostructures.[57,58] However, advanced fabrication techniques such as ion-beam milling are ultimately limited by the grain defects of the polycrystalline material itself, which at this scale critically limits the accuracy that can be achieved. In this respect, a further option to be considered that could achieve even higher quality structures would be the use of single-crystalline material as a starting point for fabrication of nanostructures.[59] Ultimately, schemes exploiting sensitivity of SHG properties to symmetry breaking of the local environment could be of interest, e.g., as modalities for optical sensing, as nonlinear scattering has been shown to be more sensitive to local refractive index changes than linear properties.[60,61] Also the rational design of nanoscale asymmetries could result in significant enhancement of the efficiency of nonlinear antennas for parametric light sources.[18,19,31]

CONCLUSIONS

In conclusion, we have shown experimentally and through simulations that both the intensity and polarization of the emitted SHG are highly sensitive to the coupling between the antenna arms. By combining single-particle linear and nonlinear microscopy and microscopic modeling accounting for the nanoscale nonlinear surface dipole distribution, the role of the surface plasmon eigenmodes and the morphology of the antennas were independently addressed. Both experiments and microscopic modeling showed qualitative overall agreement with tensor symmetry rules, but revealed deviations in parts of the parameter space showing that full electrodynamical calculations are required to quantitatively understand the SHG response. By analyzing the balance between local energy concentration and cancellation of nonlinear dipoles in the nanometer-scale gap, it is understood that for narrow gaps the SHG becomes extremely sensitive to small variations in the local symmetry of the nanostructure as more energy is drawn into the nanogap. We indeed observe such a strong variation of the SHG intensity and polarization experimentally for antennas with similar design parameters for small gaps, revealing the large role of small irregularities in the fabricated antennas in the overall SHG response. Further control over local field enhancement and nanogaps requires a next generation of tools and materials with improved accuracy and reduced defects, for example using single-crystalline materials, which may fully exploit the delicate balance of local field enhancement and cancellations of SHG at the nanoscale for applications.

EXPERIMENTAL SECTION

Nanoantenna Fabrication. Nanoantennas were fabricated by electron beam lithography (JEOL 9300FS) at an accelerating voltage of 100 kV and a writing current of 1 nA. The borofloat glass substrate was coated with a MMA (250 nm)/PMMA (150 nm) bilayer resist. A 20 nm thick conducting copolymer layer (Espacer 300Z) was used to prevent charging during electron beam exposure. After exposure, the resist was developed in methyl isobutyl ketone/isopropyl alcohol (1:1) for 60 s. The 2 nm Cr and 50 nm Au thick films were evaporated at a pressure of 5×10^6 mbar. The lift-off was done manually by soaking in *N*-methyl-2-pyrrolidone for 20 min. Selected antennas were milled using a Zeiss OrionPLUS helium ion microscope operating at 30 keV voltage, 0.9 nA current, 10 μm aperture, and 10 μs dwell time. Gaps in the L-shape were milled using 600 repeats of the base dose of 6.154 ions/cm^2 at a spot size of 1 nm and a designed gap width of 5 nm. The high aspect ratio of the cut resulted in actual gap widths of around 10 ± 2 nm.

Linear Optical Characterization. The linear optical properties of all the antennas investigated in this work have systematically been characterized using spatial modulation spectroscopy (SMS) following the method presented in ref 37. Light from a broadband supercontinuum source (Fianium) was spectrally filtered and was focused onto the sample using an achromatic Cassegrain reflective objective with a numerical

DOI: 10.1021/acsphotonics.5b00358
ACS Photonics 2015, 2, 1592−1601

aperture (NA) of 0.5. The setup covers a broad spectral range in the near-infrared from 700 to 1800 nm. The input polarization was defined using a polarization filter. Light reflected from the metallic antennas was collected and analyzed using a second polarizer.[37] A drawing of the SMS setup is shown in the Supporting Information Figure S1.

SHG Experiment. The second-harmonic generation from L-shaped antennas has been investigated on a homemade nonlinear optical microscope. Light from a femtosecond oscillator (Coherent, Chameleon Ultra II, 80 MHz, 680−1080 nm, 150 fs) is focused on the metallic antennas using a 50×, NA = 0.8 microscope objective. Nonlinear emission was collected in epi-collection, separated from the incident infrared excitation using a dichroic mirror, and sent to a photodetector (photomultiplier tube operated in analog detection mode). The signal was spectrally filtered using two different types of filters: a broadband low-pass filter (BG39) and a narrow bandpass filter centered at the SHG wavelength (typically 10 nm spectral width). A drawing of the experimental setup is presented in Supporting Information Figure S5.

Nonlinear Scattering Model. A detailed discussion of the nonlinear scattering model is presented in Supporting Information Section S3. In short, electric field distributions 5 nm inside from the nanoparticle surface were calculated with COMSOL 4.4b using an adaptive mesh with very fine meshing of the surface in the gap region down to 0.1 nm separation. Very fine meshing was necessary to achieve sufficient convergence of SHG for small capacitive antenna gaps of <20 nm. Subsequently, the nonlinear dipoles $\mathbf{p}_{NL}(\mathbf{r}, 2\omega)$ at each surface discretization cell were obtained from the square of the (complex) field component normal to the surface multiplied by the nonlinear susceptibility $\chi^{(2)}_{nnn}$:

$$\mathbf{p}_{NL}(\mathbf{r}, 2\omega) = \chi^{(2)}_{nnn}\mathbf{E}_n(\mathbf{r}, \omega)^2\,\mathbf{n}(\mathbf{r}) \quad (1)$$

Finally, the radiation from each nonlinear dipole was propagated into the far field to obtain the total SHG intensity. As the nonlinear sources are complex, the phase information that governs the far-field radiation is taken into account in our calculations. Both the influence of the substrate and numerical aperture of the microscope objective are included in the simulations, as explained in Supporting Information Section S3. A comprehensive comparison of the SHG associated with different components, $\chi^{(2)}_{npp}$ and $\chi^{(2)}_{ppn}$, of the nonlinear susceptibility tensor is provided in Supporting Information Section 3.2.

■ ASSOCIATED CONTENT

Supporting Information

The Supporting Information is available free of charge on the ACS Publications website at DOI: 10.1021/acsphotonics.5b00358.

Details on the nanoantenna fabrication method, the linear and nonlinear optical microscopy experiments, and the microscopic model of second-harmonic generation from plasmonic nanoantennas (PDF)

■ AUTHOR INFORMATION

Corresponding Authors

*E-mail: O.Muskens@soton.ac.uk.
*E-mail: arbouet@cemes.fr.

Author Contributions

§L.-J. Black and P. R. Wiecha contributed equally.

Notes

The authors declare no competing financial interest.

■ ACKNOWLEDGMENTS

This work was supported by the computing facility center CALMIP of the University Paul Sabatier of Toulouse, France. This work was supported by DSTL and DGA through a joint UK−France Ph.D. studentship and by EPSRC through grant EP/J011797/1. O.L.M. acknowledges support through EPSRC fellowship EP/J016918/1. A.A. acknowledges support from the ANR through grant ANR-14-CE26-0013. The dataset for this work can be found at 10.5258/SOTON/382840.

■ REFERENCES

(1) Muhlschlegel, P.; Eisler, H.-J.; Martin, O. J. F.; Hecht, B.; Pohl, D. W. Resonant Optical Antennas. *Science* **2005**, *308*, 1607−1609.
(2) Ghenuche, P.; Cherukulappurath, S.; Taminiau, T. H.; van Hulst, N. F.; Quidant, R. Spectroscopic Mode Mapping of Resonant Plasmon Nanoantennas. *Phys. Rev. Lett.* **2008**, *101*, 116805.
(3) Biagioni, P.; Huang, J.-S.; Hecht, B. Nanoantennas for visible and infrared radiation. *Rep. Prog. Phys.* **2012**, *75*, 024402.
(4) Willets, K. A.; Van Duyne, R. P. Localized Surface Plasmon Resonance Spectroscopy and Sensing. *Annu. Rev. Phys. Chem.* **2007**, *58*, 267−297.
(5) Curto, A. G.; Volpe, G.; Taminiau, T. H.; Kreuzer, M. P.; Quidant, R.; van Hulst, N. F. Unidirectional Emission of a Quantum Dot Coupled to a Nanoantenna. *Science* **2010**, *329*, 930−933.
(6) Knight, M. W.; Sobhani, H.; Nordlander, P.; Halas, N. J. Photodetection with Active Optical Antennas. *Science* **2011**, *332*, 702−704.
(7) Lamprecht, B.; Leitner, A.; Aussenegg, F. R. SHG Studies of Plasmon Dephasing in Nanoparticles. *Appl. Phys. B: Lasers Opt.* **1999**, *68*, 419−423.
(8) Bouhelier, A.; Beversluis, M.; Hartschuh, A.; Novotny, L. Near-Field Second-Harmonic Generation Induced by Local Field Enhancement. *Phys. Rev. Lett.* **2003**, *90*, 013903.
(9) Hubert, C.; Billot, L.; Adam, P.-M.; Bachelot, R.; Royer, P.; Grand, J.; Gindre, D.; Dorkenoo, K. D.; Fort, A. Role of Surface Plasmon in Second Harmonic Generation from Gold Nanorods. *Appl. Phys. Lett.* **2007**, *90*, 181105.
(10) Accanto, N.; Piatkowski, L.; Renger, J.; van Hulst, N. F. Capturing the Optical Phase Response of Nanoantennas by Coherent Second-Harmonic Microscopy. *Nano Lett.* **2014**, *14*, 4078−4082.
(11) Viarbitskaya, S.; Demichel, O.; Cluzel, B.; Colas des Francs, G. A. B. Delocalization of Nonlinear Optical Responses in Plasmonic NanoantennasPhys. Rev. Lett. accepted for publication.
(12) Linnenbank, H.; Linden, S. Second harmonic generation spectroscopy on second harmonic resonant plasmonic metamaterials. *Optica* **2015**, *2*, 698−701.
(13) Metzger, B.; Gui, L.; Fuchs, J.; Floess, D.; Hentschel, M.; Giessen, H. Strong Enhancement of Second Harmonic Emission by Plasmonic Resonances at the Second Harmonic Wavelength. *Nano Lett.* **2015**, *15*, 3917−3922.
(14) Lippitz, M.; van Dijk, M. A.; Orrit, M. Third-Harmonic Generation from Single Gold Nanoparticles. *Nano Lett.* **2005**, *5*, 799−802.
(15) Hentschel, M.; Utikal, T.; Giessen, H.; Lippitz, M. Quantitative Modeling of the Third Harmonic Emission Spectrum of Plasmonic Nanoantennas. *Nano Lett.* **2012**, *12*, 3778−3782.
(16) Danckwerts, M.; Novotny, L. Optical Frequency Mixing at Coupled Gold Nanoparticles. *Phys. Rev. Lett.* **2007**, *98*, 026104.
(17) Dombi, P.; Hörl, A.; Rácz, P.; Márton, I.; Trügler, A.; Krenn, J. R.; Hohenester, U. Ultrafast Strong-Field Photoemission from Plasmonic Nanoparticles. *Nano Lett.* **2013**, *13*, 674−678.

DOI: 10.1021/acsphotonics.5b00358
ACS Photonics 2015, 2, 1592−1601

(18) Hasan, S. B.; Lederer, F.; Rockstuhl, C. Nonlinear plasmonic antennas. *Mater. Today* **2014**, *17*, 478−485.
(19) Harutyunyan, H.; Volpe, G.; Quidant, R.; Novotny, L. Enhancing the Nonlinear Optical Response Using Multifrequency Gold-Nanowire Antennas. *Phys. Rev. Lett.* **2012**, *108*, 217403.
(20) Aouani, H.; Navarro-Cia, M.; Rahmani, M.; Sidiropoulos, T. P. H.; Hong, M.; Oulton, R. F.; Maier, S. A. Multiresonant Broadband Optical Antennas As Efficient Tunable Nanosources of Second Harmonic Light. *Nano Lett.* **2012**, *12*, 4997−5002.
(21) Celebrano, M.; Wu, X.; Baselli, M.; Grossmann, S.; Biagioni, P.; Locatelli, A.; De Angelis, C.; Cerullo, G.; Osellame, R.; Hecht, B.; Duò, L.; Ciccacci, F.; Finazzi, M. Ultrafast Nonlinear Control of Progressively Loaded, Single Plasmonic Nanoantennas Fabricated Using Helium Ion Milling. *Nat. Nanotechnol.* **2015**, *10*, 412−417.
(22) Thyagarajan, K.; Butet, J.; Martin, O. J. F. Augmenting Second Harmonic Generation Using Fano Resonances in Plasmonic Systems. *Nano Lett.* **2013**, *13*, 1847−1851.
(23) Metzger, B.; Schumacher, T.; Hentschel, M.; Lippitz, M.; Giessen, H. Third Harmonic Mechanism in Complex Plasmonic Fano Structures. *ACS Photonics* **2014**, *1*, 471−476.
(24) Ginzburg, P.; Krasavin, A.; Sonnefraud, Y.; Murphy, A.; Pollard, R. J.; Maier, S. A.; Zayats, A. V. Nonlinearly coupled localized plasmon resonances: Resonant second-harmonic generation. *Phys. Rev. B: Condens. Matter Mater. Phys.* **2012**, *86*, 085422.
(25) Klein, M. W.; Enkrich, C.; Wegener, M.; Linden, S. Second-Harmonic Generation from Magnetic Metamaterials. *Science* **2006**, *313*, 502−504.
(26) Feth, N.; Linden, S.; Klein, M. W.; Decker, M.; Niesler, F. B. P.; Zeng, Y.; Hoyer, W.; Liu, J.; Koch, S. W.; Moloney, J. V.; Wegener, M. Second-Harmonic Generation from Complementary Split-Ring Resonators. *Opt. Lett.* **2008**, *33*, 1975−1977.
(27) Niesler, F. B. P.; Feth, N.; Linden, S.; Niegemann, J.; Gieseler, J.; Busch, K.; Wegener, M. Second-Harmonic Generation from Split-Ring Resonators on a GaAs Substrate. *Opt. Lett.* **2009**, *34*, 1997−1999.
(28) Campione, S.; Benz, A.; Sinclair, M. B.; Capolino, F.; Brener, I. Second Harmonic Generation from Metamaterials Strongly Coupled to Intersubband Transitions in Quantum Wells. *Appl. Phys. Lett.* **2014**, *104*, 131104.
(29) Lee, J.; Tymchenko, M.; Argyropoulos, C.; Chen, P.-Y.; Lu, F.; Demmerle, F.; Boehm, G.; Amann, M.-C.; Alu, A.; Belkin, M. A. Giant Nonlinear Response from Plasmonic Metasurfaces Coupled to Intersubband Transitions. *Nature* **2014**, *511*, 65−69.
(30) Butet, J.; Lovera, A.; Martin, O. J. F. Detecting the Trapping of Small Metal Nanoparticles in the Gap of Nanoantennas with Optical Second Harmonic Generation. *Opt. Express* **2013**, *21*, 28710−28718.
(31) Dong, Z.; Asbahi, M.; Lin, J.; Zhu, D.; Wang, Y. M.; Hippalgaonkar, K.; Chu, H.-S.; Goh, W. P.; Wang, F.; Huang, Z.; Yang, J. K. W. Second-Harmonic Generation from Sub-5 nm Gaps by Directed Self-Assembly of Nanoparticles onto Template-Stripped Gold Substrates. *Nano Lett.* **2015**, *15*, 5976−5981.
(32) Palomba, S.; Novotny, L. Near-Field Imaging with a Localized Nonlinear Light Source. *Nano Lett.* **2009**, *9*, 3801−3804.
(33) Abb, M.; Wang, Y.; De Groot, C. H.; Muskens, O. L. Hotspot-Mediated Ultrafast Nonlinear Control of Multifrequency Plasmonic Nanoantennas. *Nat. Commun.* **2014**, *5*, 4869.
(34) Rodrigo, S.; Harutyunyan, H.; Novotny, L. Coherent Control of Light Scattering from Nanostructured Materials by Second-Harmonic Generation. *Phys. Rev. Lett.* **2013**, *110*, 177405.
(35) Smythe, E. J.; Cubukcu, E.; Capasso, F. Optical Properties of Surface Plasmon Resonances of Coupled Metallic Nanorods. *Opt. Express* **2007**, *15*, 7439−7447.
(36) Kats, M. A.; Genevet, P.; Aoust, G.; Yu, N.; Blanchard, R.; Aieta, F.; Gaburro, Z.; Capasso, F. Giant Birefringence in Optical Antenna Arrays with Widely Tailorable Optical Anisotropy. *Proc. Natl. Acad. Sci. U. S. A.* **2012**, *109*, 12364−12368.
(37) Black, L.-J.; Wang, Y.; de Groot, C. H.; Arbouet, A.; Muskens, O. L. Optimal Polarization Conversion in Coupled Dimer Plasmonic Nanoantennas for Metasurfaces. *ACS Nano* **2014**, *8*, 6390−6399.
(38) Meinzer, N.; Barnes, W. L.; Hooper, I. R. Plasmonic Meta-atoms and Metasurfaces. *Nat. Photonics* **2014**, *8*, 889−898.
(39) Valev, V. K. Characterization of Nanostructured Plasmonic Surfaces with Second Harmonic Generation. *Langmuir* **2012**, *28*, 15454−15471.
(40) Chen, S.; Li, G.; Zeuner, F.; Wong, W. H.; Pun, E. Y. B.; Zentgraf, T.; Cheah, K. W.; Zhang, S. Symmetry-Selective Third-Harmonic Generation from Plasmonic Metacrystals. *Phys. Rev. Lett.* **2014**, *113*, 033901.
(41) O'Brien, K.; Suchowski, H.; Rho, J.; Salandrino, A.; Kante, B.; Yin, X.; Zhang, X. Predicting Nonlinear Properties of Metamaterials from the Linear Response. *Nat. Mater.* **2015**, *14*, 379−383.
(42) Husu, H.; Canfield, B. K.; Laukkanen, J.; Bai, B.; Kuittinen, M.; Turunen, J.; Kauranen, M. Local-field effects in the nonlinear optical response of metamaterials. *Metamaterials* **2008**, *2*, 155−168.
(43) Czaplicki, R.; Husu, H.; Siikanen, R.; Mäkitalo, J.; Kauranen, M.; Laukkanen, J.; Lehtolahti, J.; Kuittinen, M. Enhancement of Second-Harmonic Generation from Metal Nanoparticles by Passive Elements. *Phys. Rev. Lett.* **2013**, *110*, 093902.
(44) Berthelot, J.; Bachelier, G.; Song, M.; Rai, P.; Colas des Francs, G.; Dereux, A.; Bouhelier, A. Silencing and Enhancement of Second-Harmonic Generation in Optical Gap Antennas. *Opt. Express* **2012**, *20*, 10498−10508.
(45) Canfield, B. K.; Kujala, S.; Jefimovs, K.; Svirko, Y.; Turunen, J.; Kauranen, M. A Macroscopic Formalism to Describe the Second-Order Nonlinear Optical Response of Nanostructures. *J. Opt. A: Pure Appl. Opt.* **2006**, *8*, S278.
(46) Canfield, B. K.; Husu, H.; Laukkanen, J.; Bai, B.; Kuittinen, M.; Turunen, J.; Kauranen, M. Local Field Asymmetry Drives Second-Harmnoic Generation in Noncentrosymmetric Nanodimers. *Nano Lett.* **2007**, *7*, 1251−1255.
(47) Butet, J.; Thyagarajan, K.; Martin, O. J. F. Ultrasensitive Optical Shape Characterization of Gold Nanoantennas Using Second Harmonic Generation. *Nano Lett.* **2013**, *13*, 1787−1792.
(48) Czaplicki, R.; Mäkitalo, J.; Siikanen, R.; Husu, H.; Lehtolahti, J.; Kuittinen, M.; Kauranen, M. Second-Harmonic Generation from Metal Nanoparticles: Resonance Enhancement versus Particle Geometry. *Nano Lett.* **2015**, *15*, 530−534.
(49) Finazzi, M.; Biagioni, P.; Celebrano, M.; Duò, L. Selection rules for second-harmonic generation in nanoparticles. *Phys. Rev. B: Condens. Matter Mater. Phys.* **2007**, *76*, 125414.
(50) Czaplicki, R.; Zdanowicz, M.; Koskinen, K.; Laukkanen, J.; Kuittinen, M.; Kauranen, M. Dipole Limit in Second-Harmonic Generation from Arrays of Gold Nanoparticles. *Opt. Express* **2011**, *19*, 26866−26871.
(51) Kauranen, M.; Zayats, A. V. Nonlinear Plasmonics. *Nat. Photonics* **2012**, *6*, 737−748.
(52) Butet, J.; Martin, O. J. F. Nonlinear Plasmonic Nanorulers. *ACS Nano* **2014**, *8*, 4931−4939.
(53) Bozhevolnyi, S. I.; Lozovski, V. Z. Self-consistent model for second-harmonic near-field microscopy. *Phys. Rev. B: Condens. Matter Mater. Phys.* **2000**, *61*, 11139−11150.
(54) Ginzburg, P.; Krasavin, A. V.; Wurtz, G. A.; Zayats, A. V. Nonperturbative Hydrodynamic Model for Multiple Harmonics Generation in Metallic Nanostructures. *ACS Photonics* **2015**, *2*, 8−13.
(55) Arbouet, A.; Christofilos, D.; Del Fatti, N.; Vallée, F.; Huntzinger, J. R.; Arnaud, L.; Billaud, P.; Broyer, M. Direct Measurement of the Single-Metal-Cluster Optical Absorption. *Phys. Rev. Lett.* **2004**, *93*, 127401−4.
(56) Wang, Y.; Abb, M.; Boden, S. A.; Aizpurua, J.; de Groot, C. H.; Muskens, O. L. Ultrafast Nonlinear Control of Progressively Loaded, Single Plasmonic Nanoantennas Fabricated Using Helium Ion Milling. *Nano Lett.* **2013**, *13*, 5647−5653.
(57) Melli, M.; Polyakov, A.; Gargas, D.; Huynh, C.; Scipioni, L.; Bao, W.; Ogletree, D. F.; Schuck, P. J.; Cabrini, S.; Weber-Bargioni, A. Reaching the Theoretical Resonance Quality Factor Limit in Coaxial Plasmonic Nanoresonators Fabricated by Helium Ion Lithography. *Nano Lett.* **2013**, *13*, 2687−2691.

DOI: 10.1021/acsphotonics.5b00358
ACS Photonics 2015, 2, 1592−1601

(58) Kollmann, H.; Piao, X.; Esmann, M.; Becker, S. F.; Hou, D.; Huynh, C.; Kautschor, L.; Bösker, G.; Vieker, H.; Beyer, A.; Gölzhäuser, A.; Park, N.; Vogelgesang, R.; Silies, M.; Lienau, C. Toward Plasmonics with Nanometer Precision: Nonlinear Optics of Helium-Ion Milled Gold Nanoantennas. *Nano Lett.* **2014**, *14*, 4778−4784.
(59) Huang, J.-S.; Callegari, V.; Geisler, P.; Brüning, C.; Kern, J.; Prangsma, J. C.; Wu, X.; Feichtner, T.; Ziegler, J.; Weinmann, P.; Kamp, M.; Forchel, A.; Biagioni, P.; Sennhauser, U.; Hecht, B. Atomically flat single-crystalline gold nanostructures for plasmonic nanocircuitry. *Nat. Commun.* **2010**, *1*, 150.
(60) Butet, J.; Russier-Antoine, I.; Jonin, C.; Lascoux, N.; Benichou, E.; Brevet, P.-F. Sensing with Multipolar Second Harmonic Generation from Spherical Metallic Nanoparticles. *Nano Lett.* **2012**, *12*, 1697−1701.
(61) Butet, J.; Martin, O. J. F. Refractive index sensing with Fano resonant plasmonic nanostructures: a symmetry based nonlinear approach. *Nanoscale* **2014**, *6*, 15262−15270.

DOI: 10.1021/acsphotonics.5b00358
ACS Photonics 2015, 2, 1592−1601